

# **A Rate Dependent Isotropic Damage Model for the Seismic Analysis of Concrete Dams**

**M. Cervera**

**J. Oliver**

**O. Manzoli**

# **A Rate Dependent Isotropic Damage Model for the Seismic Analysis of Concrete Dams**

**M. Cervera**

**J. Oliver**

**O. Manzoli**

**Publication CIMNE Nº 76, December 1995**

**International Center for Numerical Methods in Engineering**

**Gran Capitán s/n, 08034 Barcelona, Spain**



# A RATE DEPENDENT ISOTROPIC DAMAGE MODEL FOR THE SEISMIC ANALYSIS OF CONCRETE DAMS

M. CERVERA, J. OLIVER AND O. MANZOLI

*E. T. S. Ingenieros de Caminos, Canales y Puertos. Technical University of Catalonia  
Gran Capitán s/n, Edificio C1, 08034 Barcelona, Spain*

## SUMMARY

In this paper a rate-dependent isotropic damage model developed for the numerical analysis of concrete dams subjected to seismic excitation is presented. The model is shown to incorporate two features essential for seismic analysis: stiffness regradation upon load reversals and strain-rate sensitivity. The issue of mesh-objectivity is addressed using the concept of the 'characteristic length' of the fracture zone, to show that both the softening modulus and the fluidity parameter must depend on it to provide consistent results as the computational mesh is refined. Some aspects of the numerical implementation of the model are also treated, to show that the model can be easily incorporated in any standard non-linear finite element code. The application of the proposed model to the seismic analysis on a large gravity concrete dam shows that the structural response may vary significantly in terms of the development of damage. The inclusion of rate-sensitivity is able to reproduce the experimental observation that the tensile peak strength of concrete can be increased up to 50 % for the range of strain-rates that appear in a structural safety analysis of a dam subjected to severe seismic actions.

## 1. INTRODUCTION

As it is well known, concrete exhibits a rate dependent behavior when subjected to high rate straining, with significant increase of dynamic strengths and decrease of nonlinearity on the stress-strain response curves, when compared to those measured in static tests. This peculiar behaviour is rather important under impulsive loading, as it occurs when structures are subjected to impacts or explosions<sup>1</sup> (where straining rates  $\dot{\epsilon} > 10^{-2} s^{-1}$ ), but the phenomenon is also important for seismic excitations (rates of straining within the interval  $10^{-6} s^{-1} < \dot{\epsilon} < 10^{-1} s^{-1}$ ). As it will be shown, dynamic strength can be enhanced, with respect to the static one, up to 80 % in tension and 25 % in compression, for these strain rates.

The importance of this observed phenomenon had been recognized long time ago, and attempts were made for the constitutive laws to be able to account for it. However, its complexity and the need for some sophistication in the numerical models precluded it from common usage, the customary practice being to account for rate sensitivity by means of empirical formulas and drastic simplifying assumptions. Contributions from viscoplasticity were some of the first attempts to deal with rate dependency with theoretical consistency. Among others, Bićanić and Zienkiewicz<sup>2</sup> proposed one of these models, with similarity to the “bounding-surface” concept.

Observational experience shows that rate sensitivity is mainly due to the fact that the growth of internal microcracking (for a particular level of strain) is retarded at high strain rates.<sup>3</sup> Being known that for concrete (and other geomaterials) damage is essentially due to the nucleation and growth of microvoids and microcracks, it is understandable that a diminishing of microcracking with increasing strain rate will induce a reduction in macroscopic nonlinear behavior, and an increase of dynamic strengths. More recently, experimental and theoretical contributions have been introduced,<sup>4–7</sup> which provided scientific tools for dealing with this phenomenon in a realistic manner.

Starting from the observed evidence that this particular behavior is in fact consequence of the above described strain-rate dependency of the internal damage evolution, material models based on the Continuum Damage Mechanics Theory (CDMT) have been proposed. This theory was firstly introduced in the context of creep-related problems, but it has afterwards been accepted as a valid alternative to deal with complex material behaviour. It is nowadays used for materials so different as metals, ceramics, rock and concrete, and within a wide range of applications (creep, fatigue, progressive failure, etc.). The reason for its popularity is as much the intrinsic simplicity and versatility of the approach, as well as its consistency, based on the theory of thermodynamics of irreversible processes. Among the different possibilities that such a framework offers, this work will make use of an *isotropic damage model*, with only two scalar internal variables to monitor the local damage under tension and compression, respectively. This will provide a simple constitutive model which, nevertheless, is able to capture the overall non-linear behaviour of concrete displayed under seismic loading, including the strain-softening response, the stiffness degradation and regradation observed under multiple stress reversals and the experimentally observed strain-rate dependency. Furthermore, the model can be implemented in a strain-driven form which leads to an almost closed-form algorithm to integrate the stress tensor in time. This is a most valuable feature for a model intended to be used in large scale computations.

Following this approach, this paper is organised as follows. Section 2 describes a rate-independent constitutive model for concrete based on CDMT which allows for independent tension and compression damage and exhibits stiffness recovery upon load reversals. Section 3 describes a viscous regularization of the proposed model to account for rate-dependent effects. Section 4 deals with the numerical implementation of both models in a standard FEM framework. Section 5 presents some numerical examples to show the performance of the model. Section 6 presents the application of the proposed models to the seismic analysis of a gravity dam subjected to seismic excitation. Section 7 closes the paper with some conclusions on the proposed model.

## 2. RATE INDEPENDENT MODEL

The Continuum Damage Mechanics Theory (CDMT) is based on the definition of the effective stress concept, which is introduced in connection with the hypothesis of strain equivalence<sup>8</sup>: the strain associated with a damaged state under the applied stress  $\sigma$  is equivalent to the strain associated with its undamaged state under the effective stress  $\bar{\sigma}$ . In the present work the effective stress tensor  $\bar{\sigma}$  (second order) will assume the following form:

$$\bar{\sigma} = \mathbf{D}_0 : \epsilon \quad (1)$$

In this expression  $\mathbf{D}_0$  is the usual fourth order linear-elastic constitutive matrix,  $\epsilon$  is the second order strain tensor, and  $(:)$  denotes the tensorial product contracted on two indices. As our aim is to use a scalar damage model, with separated internal damage variables for tensile and compressive stress contributions, a split of the *effective* stress tensor into tensile and compressive components is needed. In order to identify clearly contributions with respect to each one of these independent effective stress tensors, (+) and (-) indices will be extensively used, referring to tensile and compressive entities, respectively. In this work, the stress split will be performed as<sup>9</sup>:

$$\begin{aligned} \bar{\sigma}^+ &= \langle \bar{\sigma} \rangle = \sum_{i=1}^3 \langle \bar{\sigma}_i \rangle \mathbf{p}_i \otimes \mathbf{p}_i \\ \bar{\sigma}^- &= \langle \bar{\sigma} \rangle^- = \sum_{i=1}^3 \langle \bar{\sigma}_i \rangle^- \mathbf{p}_i \otimes \mathbf{p}_i \end{aligned} \quad (2)$$

where  $\bar{\sigma}_i$  denotes the *i*-th principal stress value from tensor  $\bar{\sigma}$ ,  $\mathbf{p}_i$  represents the unit vector associated with its respective principal direction and the symbol  $\otimes$  denotes the tensorial product. The symbols  $\langle . \rangle$  are the Macaulay brackets (thus giving the value of the enclosed expression when positive, and setting a zero value if negative), and symbols  $\langle . \rangle^-$  are such that  $\langle x \rangle^- + \langle x \rangle = x$ .

Hence, according to this stress splitting, the constitutive law proposed in this work can be defined explicitly, rendering for the Cauchy stress tensor  $\sigma$  the final expression:

$$\sigma = (1 - d^+) \bar{\sigma}^+ + (1 - d^-) \bar{\sigma}^- \quad (3.a)$$

with

$$0 \leq d^+ \leq 1 \quad \text{and} \quad 0 \leq d^- \leq 1 \quad (3.b)$$

where  $d^+$  and  $d^-$  are the tensile and compressive damage variables, respectively. Thermodynamic considerations about the non-negativeness of the dissipation<sup>9</sup> demand that  $\dot{d}^+ \geq 0$  and  $\dot{d}^- \geq 0$ . The model is completed with appropriate evolution laws for these internal damage variables.

It is worth noting that Eq. (3) characterizes the full stress tensor, and therefore, the two damage variables control the degradation of all the elastic properties that describe the material: Young's modulus, Poisson's ratio, shear modulus, etc. Thus, the model is not

only devised to predict mode I failures, but it can also deal with mixed failures (modes I and II). It may also be remarked that Eq. (3) defines an isotropic model. Although CDMT can accommodate anisotropic models and they are often justified in the literature by macroscopic damage observations, there is some doubt about their consistency with thermodynamic principles when opening and closure of the cracks (damage areas) occur during the load history<sup>10</sup>. In the context of strong discontinuity modelling, it has been shown<sup>11</sup> that isotropic models can deal with anisotropic directional damage in a consistent manner.

In order to clearly define concepts such as loading, unloading, or reloading, a scalar positive quantity, termed *equivalent stress*, will be defined. This permits a comparison of different tridimensional stress states. With such a definition, distinct tridimensional stress states can be mapped to a single *equivalent* unidimensional stress test, which makes possible their quantitative comparison. As a consequence of the stress split, an equivalent effective tensile norm  $\bar{\tau}^+$  and an equivalent effective compressive norm  $\bar{\tau}^-$  will be used. In the present work they will assume the following forms:

$$\bar{\tau}^+ = \sqrt{\bar{\sigma}^+ : \mathbf{D}_0^{-1} : \bar{\sigma}^+} \quad (4.a)$$

$$\bar{\tau}^- = \sqrt{\sqrt{3} (K \bar{\sigma}_{oct}^- + \bar{\tau}_{oct}^-)} \quad (4.b)$$

In Eq. (4.b)  $\bar{\sigma}_{oct}^-$  and  $\bar{\tau}_{oct}^-$  are, respectively, the octahedral normal stress and the octahedral shear stress, obtained from  $\bar{\sigma}^-$ ;  $K$  is a material property which depends on the ratio between the biaxial and uniaxial compressive strengths of the concrete,  $\beta$ , so that  $K = \sqrt{2}(\beta - 1)/(2\beta - 1)$  (typical values for concrete are  $\beta = 1.16$ ,  $K = 0.171$ ).

With the above definitions for the effective equivalent norms, two separated damage criteria  $g^+$  and  $g^-$  will be introduced,<sup>12</sup> the former for tension and the latter for compression:

$$g^+(\bar{\tau}^+, r^+) = \bar{\tau}^+ - r^+ \leq 0 \quad (5.a)$$

$$g^-(\bar{\tau}^-, r^-) = \bar{\tau}^- - r^- \leq 0 \quad (5.b)$$

Variables  $r^+$  and  $r^-$  are current damage thresholds, in the sense that their values control the size of the expanding damage surfaces. For the initial stage, that is, when no loading has yet been applied, values  $r_0^+$  and  $r_0^-$  (assumed material properties related to the uniaxial tensile and compressive peak strengths) are attributed to these thresholds. As it can be deduced from definitions (4.a) and (4.b), Eq. (5.a) corresponds to a damage bounding surface which is an ellipsoid centered at the origin in the space of principal undamaged tensile stresses,<sup>13</sup> and Eq. (5.b) defines a Drucker-Prager cone for compression. Eq. (5.a) states that tensile damage tends to increase if  $\bar{\tau}^+ = r^+$ , and so it will be initiated when for the first time  $\bar{\tau}^+ = r_0^+$  (a similar reasoning can be applied for compression). Figure 1 shows the initial damage bounding surface resulting from the combination of both criteria in a biaxial effective principal stress space. Note the good qualitative agreement with the documented experimental results for concrete.

With these definitions, and after enforcement of the consistency conditions for loading, unloading and reloading situations via the Kuhn–Tucker relations, the kinematics of the tensile and compressive internal variables are defined as<sup>12</sup>:

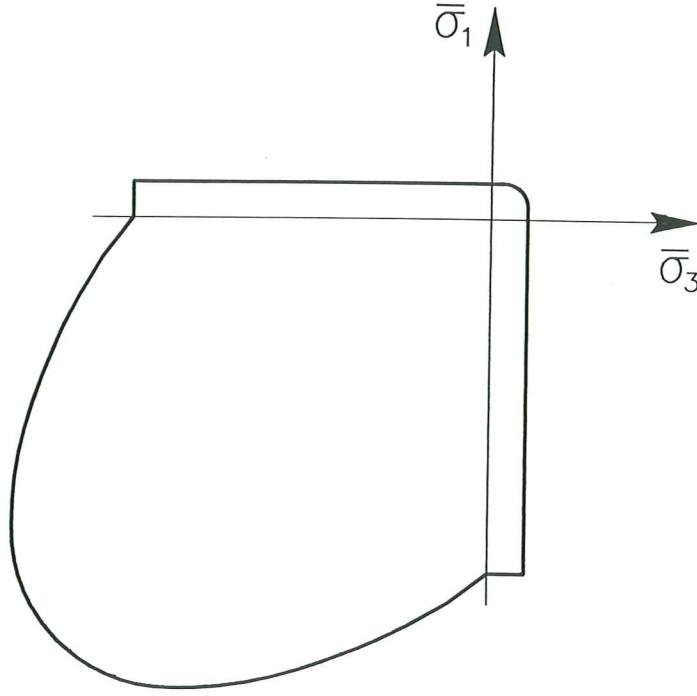


Figure 1. Initial damage bounding surface in a biaxial effective principal stress space

$$\dot{r}^+ = \dot{\bar{\tau}}^+ \geq 0 \quad \dot{d}^+ = \dot{r}^+ \frac{\partial G^+(r^+)}{\partial r^+} = \dot{G}^+(r^+) \geq 0 \quad (6.a)$$

$$\dot{r}^- = \dot{\bar{\tau}}^- \geq 0 \quad \dot{d}^- = \dot{r}^- \frac{\partial G^-(r^-)}{\partial r^-} = \dot{G}^-(r^-) \geq 0 \quad (6.b)$$

with  $G^+$  and  $G^-$  being appropriate monotone-increasing functions derived from experimental observation. The particular forms assumed by the rate Eqs. (6.a) and (6.b) allow the specification of the following damage evolution laws, after performing a trivial integration (with the initial condition of null damages):

$$r^+ = \max(r_0^+, \max(\bar{\tau}^+)) \quad d^+ = G^+(r^+) \quad (7.a)$$

$$r^- = \max(r_0^-, \max(\bar{\tau}^-)) \quad d^- = G^-(r^-) \quad (7.b)$$

These equations put into evidence that the (rate-independent) model is strain driven in a closed form: once the current strain tensor,  $\epsilon$ , is known, damage variables can be easily evaluated, as they only depend on the equivalent norms  $\bar{\tau}^+$  and  $\bar{\tau}^-$ , which are evaluated from  $\epsilon$ . So, the selection for the particular forms of functions  $G^+$  and  $G^-$  will determine the specific damage evolutions to be considered, and consequently some care must be devoted to this subject, so that a realistic representation of experimental behavior might be obtained. Anyway, the change from one particular set of evolution laws to a different one does not put any special problem, thus enabling this model to have substantial updating versatility.



For the present work, the following damage evolution rules will be adopted:

$$d^+ = 1 - \frac{r_0^+}{r^+} e^{A^+ \left(1 - \frac{r^+}{r_0^+}\right)} \quad (8.a)$$

$$d^- = 1 - \frac{r_0^-}{r^-} \left(1 - A^-\right) - A^- e^{B^- \left(1 - \frac{r^-}{r_0^-}\right)} \quad (8.b)$$

Eq. (8.a) is able to reproduce the softening branch of a concrete unidimensional tensile test, asymptotically to the strain axis. With this evolution law for  $d^+$ , a finite area is retained between the stress-strain curve and the strain axis. This area defines the available energy to be dissipated in the control volume. As it is well known, this energy has to be appropriately related to the fracture energy of concrete (regarded to be a material property) to satisfy the requisites of mesh-objectivity when dealing with softening materials.<sup>11,13</sup> The fundamental issue here is the introduction of a geometrical factor,  $l_{ch}$ , called *characteristic length*, which depends on the spatial discretization and ensures conservation of the energy dissipated by the material.<sup>14</sup> Therefore, the determination of the parameter  $A^+$  is made by equating the material fracture energy *per unit of characteristic length* to the time integral of dissipation, to render<sup>9</sup> (see Appendix):

$$\frac{1}{A^+} = \frac{1}{2\bar{H}^+} \left( \frac{1}{l_{ch}} - \bar{H}^+ \right) \geq 0 \quad (9)$$

where  $\bar{H}^+ = (r_0^+)^2/2G_f^+ = (f_0^+)^2/2EG_f^+$  depends on the material properties, as  $G_f^+$  is the (tensile) fracture energy per unit area,  $f_0^+$  is the uniaxial tensile strength and  $E$  is the elastic modulus. In the framework of *local* models and finite element analysis, the state variables are computed at the integration points in terms of the local strain (and/or stress) history. Therefore, the threshold and damage internal variables are defined at the integration points. The characteristic length is thus related to the volume (or area) of each finite element. In this work its value will be approximated by the cubic (or square) root of this volume (or area). It is clear from Eq. (9) that the introduction of the characteristic length implies a limitation on the maximum size of the finite elements used in the mesh,  $l_{ch} \leq 1/\bar{H}^+$ . The greater the elements, the steeper is the softening branch of the response, and, locally, the fracture process is more brittle.

By means of Eq. (8.b) it is possible to reproduce the hardening effect on concrete subjected to compression, as well the softening which occurs after the compressive strength is attained. Besides  $r_0^-$ , for its characterization two parameters ( $A^-$ ,  $B^-$ ) must be defined, usually by imposing that the evolution curve satisfies two selected points of a unidimensional experimental test. If softening is also contemplated under compressive strains, these parameters must also be related to the characteristic length and to the (compressive) fracture energy.

### 3. RATE DEPENDENT MODEL

As mentioned in the introduction, there is a strong coupling between nonlinear rate-sensitivity in concrete (and other geomaterials) and damage growth. Therefore, it is natural to develop a rate dependent constitutive model within the framework of CDMT, evolving from the above presented rate independent damage model, and which accounts for strain rate dependency via the damage evolution laws.

As the final goal of this work is to capture the seismic response of concrete dams (large scale structures), emphasis is placed in the obtention of a model which is strain driven (and thus, suitable for application within the Finite Element Method) and where the constitutive relationship can be integrated as efficiently as possible (and thus, being feasible for large size computations).

To this end, let us consider a viscous regularization of the rate-independent damage thresholds evolution laws defined by the left-hand side of Eqs. (6), so that these are replaced by:

$$\dot{r}^+ = \vartheta^+ \phi^+(\bar{\tau}^+ - r^+) \geq 0 \quad \dot{d}^+ = \dot{r}^+ \frac{\partial G^+(r^+)}{\partial r^+} = \dot{G}^+(r^+) \geq 0 \quad (10.a)$$

$$\dot{r}^- = \vartheta^- \phi^-(\bar{\tau}^- - r^-) \geq 0 \quad \dot{d}^- = \dot{r}^- \frac{\partial G^-(r^-)}{\partial r^-} = \dot{G}^-(r^-) \geq 0 \quad (10.b)$$

where  $\phi^+$  and  $\phi^-$  are dimensionless scalar functions called the viscous damage threshold flow functions;  $\vartheta^+$  and  $\vartheta^-$  are the fluidity parameters. Note that the modification of the evolution laws only affects the integration of the damage thresholds ( $r^+$  and  $r^-$ ), but not the damage variables ( $d^+$  and  $d^-$ ) themselves. These are still obtained in a closed form, through the explicit definition of the functions  $G^+(r^+)$  and  $G^-(r^-)$ . Additionally, it is worth to remark that, since Eqs. (10) guarantee monotone increasing damage variables ( $\dot{d}^+ \geq 0$  and  $\dot{d}^- \geq 0$ ), the condition of non-negative dissipation required from the thermodynamic principles is satisfied.

The viscous threshold damage flow functions may assume the following form:

$$\phi^+(\bar{\tau}^+ - r^+) = r_0^+ \left( \frac{\langle \bar{\tau}^+ - r^+ \rangle}{r^+} \right)^{a^+} \quad (11.a)$$

$$\phi^-(\bar{\tau}^- - r^-) = r_0^- \left( \frac{\langle \bar{\tau}^- - r^- \rangle}{r^-} \right)^{a^-} \quad (11.b)$$

Note that  $a^+$ ,  $a^-$  are positive exponents, also supposed to be material properties. The determination of these exponents, as well as that of the fluidity parameters is done by means of uniaxial tensile and compressive tests. Note that different values can be attributed to the tensile and compressive parameters and exponents, and this will allow to account for the different rate sensitivities (greater under tensile than under compressive loading) exhibited by concrete.

The reasoning behind the above laws is analogous to the classical Perzina viscoplastic regularization often used in the framework of Computational Plasticity. It can be seen

that this assumed rate dependent formulation is a general form for the damage threshold and damage evolution, so that for an infinity value of the fluidity parameter, the rate-independent (or inviscid) damage evolution law is recovered, while for a zero value of  $\vartheta$ , evolution of the damage variables is prevented, thus rendering an instantaneously elastic response.

An alternative regularization of the viscous-damage model was proposed by Simo and Ju<sup>12</sup>, which can be expressed as:

$$\dot{r}^+ = \vartheta^+ \phi^+(\bar{\tau}^+ - r^+) \geq 0 \quad \dot{d}^+ = \vartheta^+ \phi^+(\bar{\tau}^+ - r^+) \frac{\partial G^+(\bar{\tau}^+)}{\partial \bar{\tau}^+} \geq 0 \quad (12.a)$$

$$\dot{r}^- = \vartheta^- \phi^-(\bar{\tau}^- - r^-) \geq 0 \quad \dot{d}^- = \vartheta^- \phi^-(\bar{\tau}^- - r^-) \frac{\partial G^-(\bar{\tau}^-)}{\partial \bar{\tau}^-} \geq 0 \quad (12.b)$$

Note firstly that here the closed form for the damage variable is lost, and thus the model is necessarily less efficient. However, the main drawback of this approach is the dependency of Eqs. (12) on  $\partial G(\bar{\tau})/\partial \bar{\tau}$ , which precludes the evolution of damage when this derivative vanishes. For a given  $G$  function, this will happen for a fixed value of  $\bar{\tau}$ , independently of the rate of straining. From the authors' point of view this makes this alternative not suitable for the modelling of the mechanical behaviour of concrete, as rate dependency would only be active for a limited range of strain.

It has been known for a number of years,<sup>15</sup> and it is evident from the analysis performed in the Appendix, that to be able to obtain mesh independent time responses exhibiting proper localization when using viscous-type models, the fluidity parameters must also be mesh dependent. Otherwise, the width of the localization band is greater than one element, and the inviscid model is not recovered as a limit case of the viscous regularization. Coming from the analysis presented in the Appendix we will assume in this work that:

$$\vartheta^+ = \bar{\vartheta}^+ \left( \frac{1}{l_{ch}} - \bar{H}^+ \right) \geq 0 \quad (13)$$

where  $\bar{\vartheta}^+$  and  $\bar{H}^+$  are material properties (see Eq. (9)) and  $l_{ch}$  is the characteristic length. A similar relationship would be adopted for  $\vartheta^-$  if softening should also be modelled under compression.

#### 4. NUMERICAL IMPLEMENTATION

A numerical algorithm needs to be implemented for the time integration of the damage constitutive equations presented in the previous sections. In the following this algorithm is presented, in a strain-driven form which leads to an almost closed-form algorithm to integrate the stress tensor in time. This is most appropriate within the context of the application of the finite element method.

Figure 2 presents the scheme followed for the evaluation of the stress tensor corresponding to a given strain tensor for each time step in a displacement-based finite element code. Each time step begins at time  $t_n$  with all state variables known and it ends at time  $t_{n+1}$

INPUT:  $r_n^+, r_n^-, \bar{\sigma}_n, \epsilon_{n+1}$

OUTPUT:  $r_{n+1}^+, r_{n+1}^-, \bar{\sigma}_{n+1}$

(1) Evaluate  $\bar{\sigma}_{n+1} = \mathbf{D}_o : \epsilon_{n+1}$

(2) Split  $\bar{\sigma}_{n+1}$  into  $\bar{\sigma}_{n+1}^+$  and  $\bar{\sigma}_{n+1}^-$  according to Eq. (2)

(3) Compute equivalent stresses  $\bar{\tau}_{n+1}^+$  and  $\bar{\tau}_{n+1}^-$  according to Eq. (4)

(4) Compute equivalent stresses  $\bar{\tau}_\alpha^+$  and  $\bar{\tau}_\alpha^-$  according to Eq. (15.a)

(5) Check for  $\bar{\tau}_\alpha^+ > r_n^+$

YES: Check for  $\vartheta^+ > 0$  (rate dependent case ?)

YES: Update threshold  $r_{n+1}^+$  according Eq. (17)

Compute  $r_\alpha^+$  according to Eq. (15.b)

If  $\bar{\tau}_\alpha^+ < r_\alpha^+$  then reset  $r_{n+1}^+ = r_n^+$

NO: Update threshold according to  $r_{n+1}^+ = \bar{\tau}_{n+1}^+$

NO: Set  $r_{n+1}^+ = r_n^+$

(6) Check for  $\bar{\tau}_\alpha^- > r_n^-$

YES: Check for  $\vartheta^- > 0$  (rate dependent case ?)

YES: Update threshold  $r_{n+1}^-$  according Eq. (17)

Compute  $r_\alpha^-$  according to Eq. (15.b)

If  $\bar{\tau}_\alpha^- < r_\alpha^-$  then reset  $r_{n+1}^- = r_n^-$

NO: Update threshold according to  $r_{n+1}^- = \bar{\tau}_{n+1}^-$

NO: Set  $r_{n+1}^- = r_n^-$

(7) Evaluate damage variables:

$$d_{n+1}^+ = G^+(r_{n+1}^+)$$

$$d_{n+1}^- = G^-(r_{n+1}^-)$$

(8) Compute final stress tensor:

$$\bar{\sigma}_{n+1} = (1 - d_{n+1}^+) \bar{\sigma}_{n+1}^+ + (1 - d_{n+1}^-) \bar{\sigma}_{n+1}^-$$

Figure 2. Algorithm for the evaluation of stresses

with the state variables updated according to the given total strain tensor  $\epsilon$ . The time step size is  $\Delta t = t_{n+1} - t_n$ .

Note that the only difference between the rate-independent and dependent models is the updating of the damage thresholds when evolution of the damage occurs, that is, upon loading conditions. For the rate-dependent model, these may be evaluated using a generalized mid-point rule to integrate Eqs. (10), i.e.,

$$r_{n+1} = r_n + \Delta t \vartheta \phi(\bar{\tau}_\alpha - r_\alpha) \quad (14)$$

where  $\bar{\tau}_\alpha$  and  $r_\alpha$  are defined by:

$$\bar{\tau}_\alpha = (1 - \alpha)\bar{\tau}_n + \alpha\bar{\tau}_{n+1} \quad (15.a)$$

$$r_\alpha = (1 - \alpha)r_n + \alpha r_{n+1} \quad (15.b)$$

Then, substitution of Eqs. (15) into Eq. (14) renders:

$$r_{n+1} = r_n + \Delta t \vartheta \phi((1 - \alpha)(\bar{\tau}_n - r_n) + \alpha(\bar{\tau}_{n+1} - r_{n+1})) \quad (16)$$

Note that for  $\alpha = 1$  Eq. (16) corresponds to a backward-Euler difference scheme. It is easy to show that the algorithm of Eq. (16) is unconditionally stable for  $\alpha \geq 0.5$  and second order accurate only for  $\alpha = 0.5$  (Crank-Nicolson or trapezoidal rule), which allows the use of larger time step sizes for rate-dependent analysis.

It is obvious that the explicit determination of  $r_{n+1}$  is possible only for small integer values of the exponent  $a$  in Eq. (11), as the cases  $a = 1, 2, 3$  lead to linear, quadratic and cubic expressions for Eq. (16), respectively. In the general case, Eq. (16) may be solved by the iterative Newton-Raphson method, which ensures a fast rate of convergence. To this purpose, Eq. (16) may be rewritten as:

$$f(r_{n+1}) = -r_{n+1} + r_n + \Delta t \vartheta \phi((1 - \alpha)(\bar{\tau}_n - r_n) + \alpha(\bar{\tau}_{n+1} - r_{n+1})) = 0 \quad (17)$$

so that the problem is now to find the root of Eq. (17) by an iterative Newton-Raphson procedure given by:

$$r_{n+1}^{i+1} = r_{n+1}^i - \frac{f(r_{n+1}^i)}{f'(r_{n+1}^i)} \quad (18)$$

where  $r_{n+1}^{i+1}$  indicates an improved approximation to the exact root obtained from the previous  $r_{n+1}^i$  approximation and  $f'$  is the first derivative of function  $f$  with respect to  $r_{n+1}$ . The iteration procedure starts for  $i = 0$  with  $r_{n+1}^0 = r_n$  and finishes when a preselected convergence criterion is satisfied.

Note that in Eq. (14) the condition to update the damage threshold is  $\bar{\tau}_\alpha > r_\alpha$ . However,  $r_\alpha$  cannot be computed before a new value for  $r_{n+1}$  is found. Therefore, the previous condition is changed in the algorithm of Figure 2 by an alternative check,  $\bar{\tau}_\alpha > r_n$ . Consequently, once a converged value for  $r_{n+1}$  has been computed according to the described procedure, Eq. (15.b) is used to evaluate the corresponding  $r_\alpha$  value. Then a check is performed to ensure that the condition  $r_\alpha > \bar{\tau}_\alpha$  is satisfied. Otherwise, there is no evolution of damage in the time step and, therefore,  $r_{n+1} = r_n$ .

## 5. NUMERICAL EXAMPLES

### 5.1 Rate independent model. Tension–Compression cyclic test

This first example is presented to demonstrate the ability of the model to simulate the characteristic tensile and compressive behaviour of concrete for slow strain–rate situations. Figure 3 shows the *calculated* cyclic behaviour of the proposed rate independent continuum damage model in a uniaxial test performed with a single finite element (4 nodes,  $l_{ch} = 1$ ) subjected to prescribed axial displacements. The figure is plotted in a non-dimensional mapped form ( $f$  versus  $e$ ) obtained by dividing the stress by the respective damage stress thresholds ( $f = \sigma/f_0^{+/-}$ ) and the strain by the respective strain thresholds ( $e = \varepsilon/(f_0^{+/-}/E)$ ). The material properties to be used here are:  $E = 30$  GPa (elastic modulus),  $\nu = 0.2$  (Poisson ratio), with a tensile strength  $f_0^+ = 2.0$  MPa and a fracture energy  $G_f = 250$  N/m, and a compression stress threshold for damage  $f_0^- = 12.0$  MPa. The corresponding parameters that define this model concrete behaviour are:  $A^+ = 0.677$ ,  $A^- = 1.000$  and  $B^- = 0.890$ .

The load sequence and the response are described as follows. The element is firstly stretched until damage in tension occurs (path  $ABC$ ); then the imposed displacements are reversed so that secant unloading, regradation of the stiffness and damage in compression occur (path  $CAD E$ ); a new reversal shows secant unloading, reloading and further damage in tension until the stress virtually vanishes (path  $EAC F$ ); a new reversal shows a new regradation of stiffness to the damaged compression one and evolution of damage under further loading (path  $FAEG$ ); the final reversal shows secant unloading to the origin (path  $GA$ ).

### 5.2 Rate dependent model. Strain–Rate dependency effect

In order to show the strain–rate dependency effect that the viscous model is able to simulate, a model concrete will be used with the same material properties as in the previous example. Figure 4 shows the stress–strain curves obtained for uniaxial tension tests performed at different strain rates (in the figure  $v = \dot{\varepsilon}$ ), using the viscous damage flow proposed in Eq. (11.a). It can be noted that for higher strain–rates the peak stress increases, which corresponds to the experimental evidence. It is also noted that the energy dissipated during the test is also larger for higher strain–rates. In the limit, for very slow straining, the rate dependent model simulates the inviscid behaviour, and it dissipates the expected fracture energy per unit length.

The additional material parameters needed for the viscous model have been calibrated to match the response of the model to the experimental *peak strength ratio versus strain–rate* curves obtained by Suaris and Shah,<sup>5</sup> where the peak strength ratio is the relation between the dynamic and static peak strengths. Figure 5 shows the comparison between the experimental and the computed peak stress values obtained with the following parameters:  $\bar{\vartheta}^+ = 870$  s<sup>-1</sup>,  $\bar{\vartheta}^- = 40000$  s<sup>-1</sup> and  $a^+ = a^- = 5$ . This values will be used throughout this work. Note the satisfactory agreement between the experimental and the analytical peak stress values.

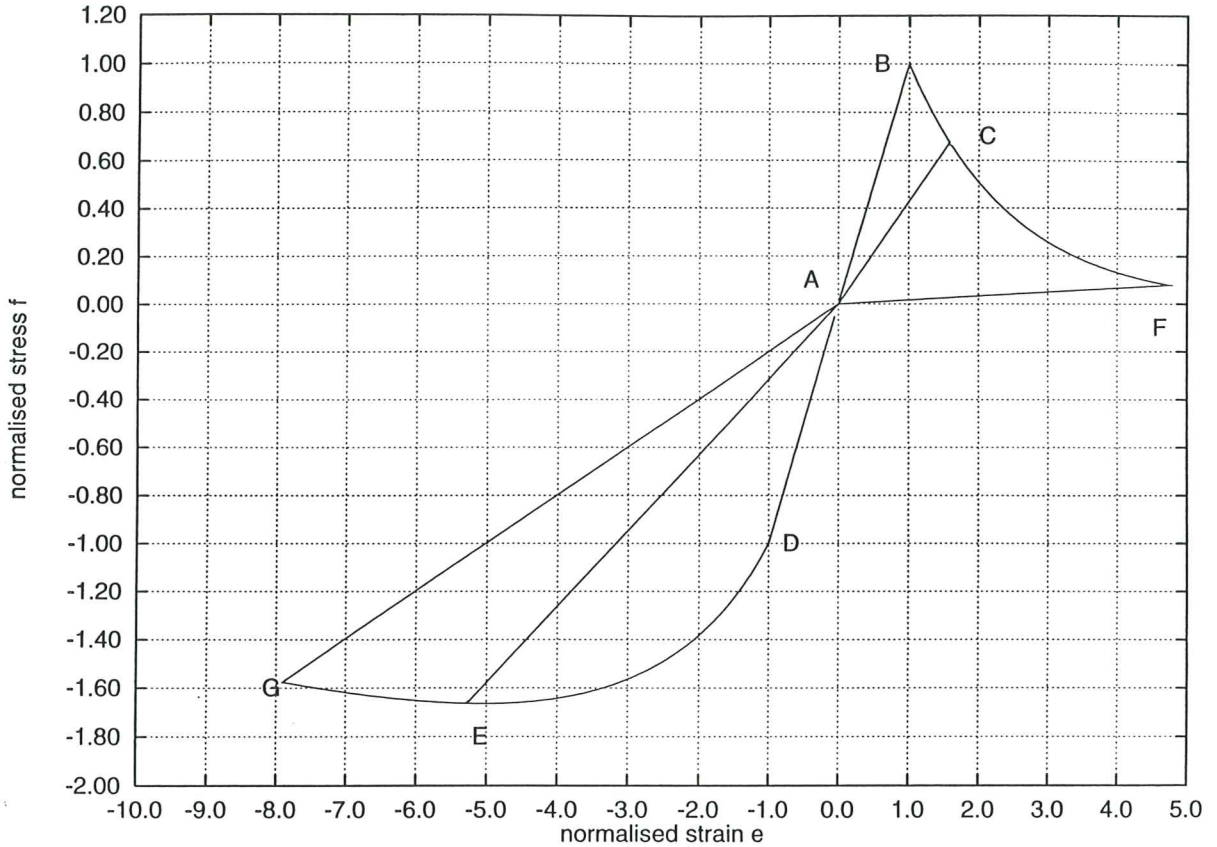


Figure 3. Cyclic behaviour of the rate independent model in a uniaxial test

### 5.3 Performance of the time integration scheme

Figure 6 shows the relative performance of the generalised mid-point time integration scheme used for the rate dependent model. This scheme is used here to track the response for a tensile uniaxial test with strain rate  $\dot{\epsilon} = 10^{-1} \text{ s}^{-1}$ . Figure (6.a) shows the curves obtained using  $\alpha = 1.0$  (backward Euler) with 100, 10 and 5 time steps. Figure (6.b) shows the same curves obtained using  $\alpha = 0.5$  (Crank-Nicolson). Although both algorithms are unconditionally stable, the second one is much more accurate (second order), and it is able to capture the peak strength with greater time step sizes.

### 5.4 Mesh independence test

Let us now consider the test problem depicted in Figure 7 for an uniaxial tension test. The test is carried out by imposing a free-end displacement  $\delta(t) = vt + \delta_0$  as a linear function of time, and with  $\delta_0 = f_0^+ l/E$ , so that  $t = 0$  is the time for the onset of damage. The material properties are the same used in previous examples. The total length of the bar is  $l$  and it is discretized using a row of  $N$  four noded elements. One of the elements is slightly perturbed so that damage will develop in a band equal to  $l_{ch}$  (the width of the perturbed element,  $l_{ch} = l/n$ ).

Figure 8 shows the results obtained for the numerical simulation of the tension test using a linear softening law (see Appendix, Eq. (A.11)) for three different straining rates

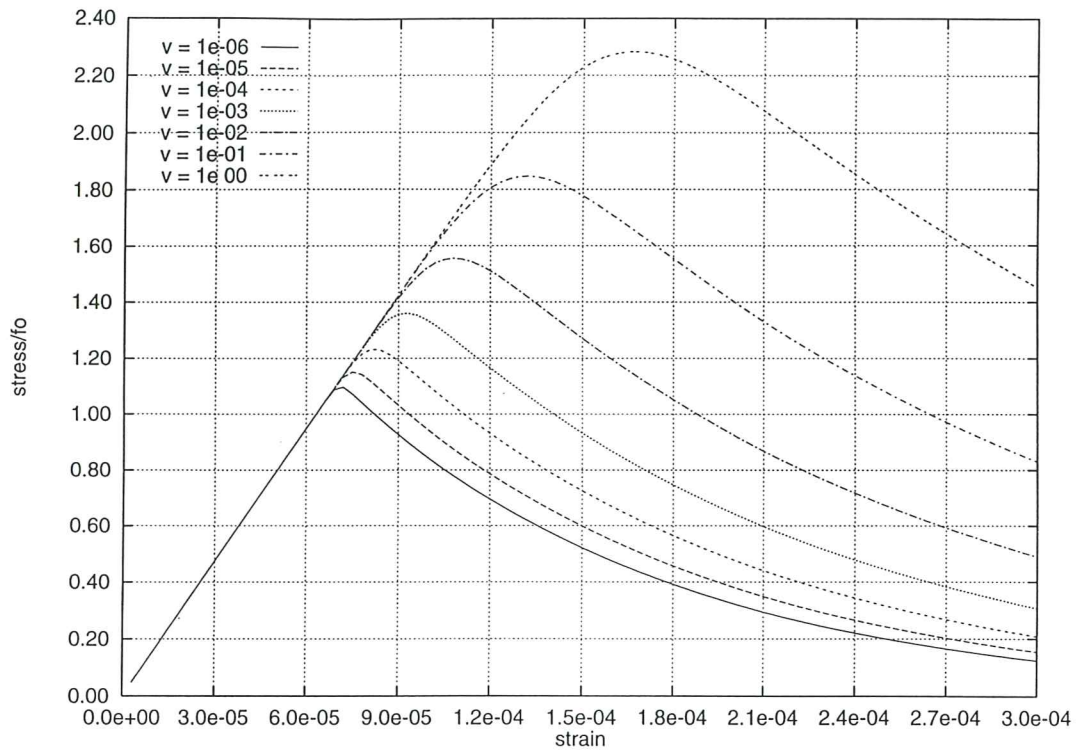


Figure 4. Strain-rate dependency effect in a tensile uniaxial test

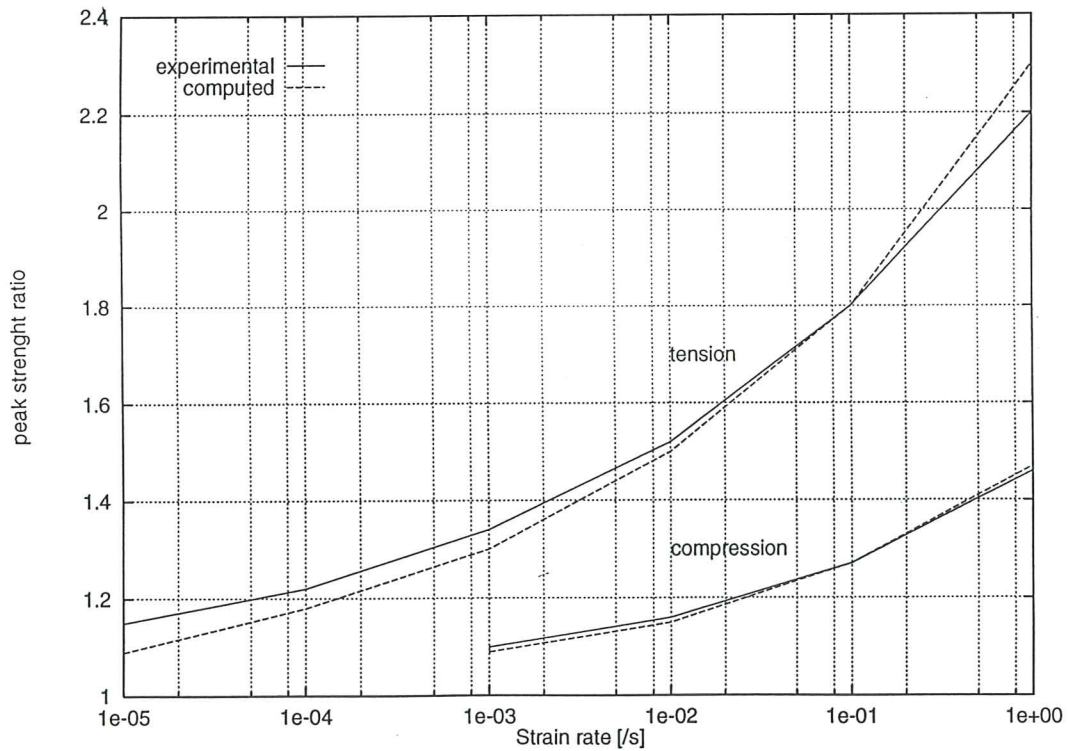


Figure 5. Calibration of Peak Strength ratio versus strain-rate



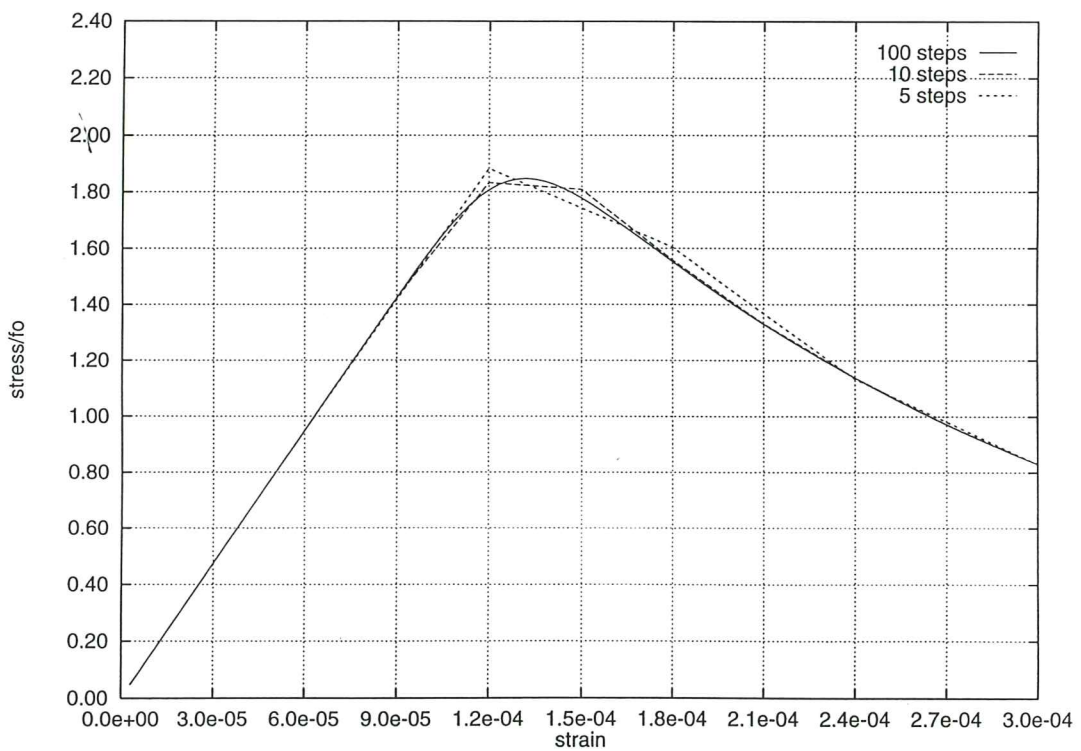
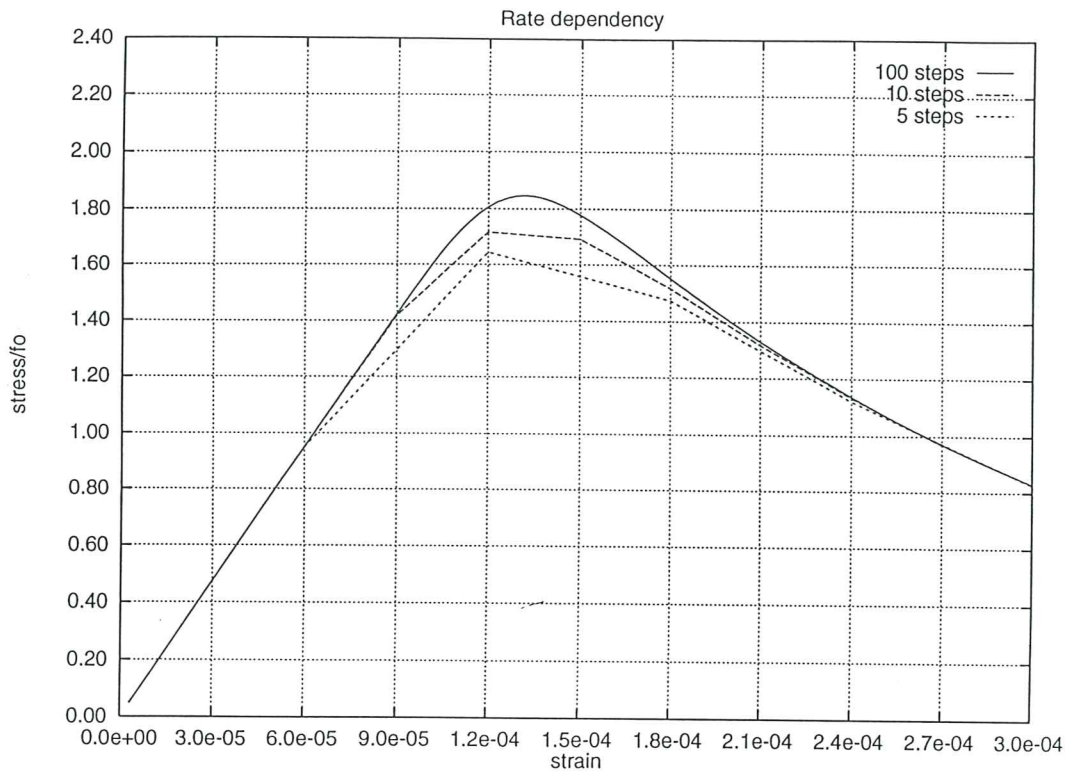


Figure 6. Performance of the time integration scheme: (a) Backward Euler, (b) Crank-Nicolson

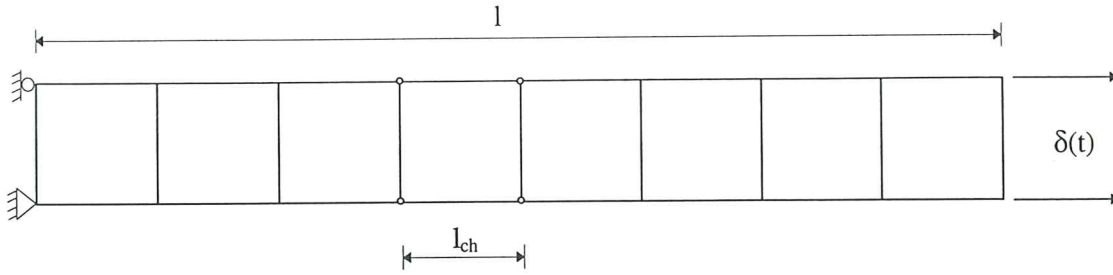


Figure 7. Uniaxial tension test problem. Geometry.

( $v = 10^{-1}, 10^{-2}$  and  $10^{-4}$  m/s) and for three different discretizations ( $n = 2, 20$  and 200 elements). As shown in the Appendix, results are mesh objective, as the curves for the different discretizations literally overlap for each straining rate. This shows that the expressions obtained for the dependence of the softening modulus and the fluidity parameters on the characteristic length are correct.

Figure 9 shows the results obtained for the numerical simulation of the tension test using an exponential softening law (see Eq. (8.a) and Appendix, Eq. (A.20)) for the same straining rates ( $v = 10^{-1}, 10^{-2}$  and  $10^{-4}$  m/s) and the same discretizations ( $n = 2, 20$  and 200 elements). As shown in the Appendix, results in this case are not exactly mesh independent, as the curves for the different discretizations do not overlap for each straining rate. However, it is very clear from the figure that results do converge on mesh refinement, and curves for  $n = 20$  and  $n = 200$  elements almost overlap and, consequently, mesh objectivity is achieved. This shows that the conclusions reached in the Appendix for the dependence of the softening modulus and the fluidity parameters on the characteristic length are correct.

## 6. SEISMIC ANALYSIS OF A GRAVITY DAM

The computational model for concrete described in the previous sections is now applied to the analysis of a concrete gravity dam subjected to seismic action. The geometry of the problem is depicted in Figure (10.a), where the foundation and the reservoir included in the numerical model are also shown. Fluid–structure interaction is dealt with in a block–iterative manner, so the ‘fluid’ and the ‘solid’ phases are in fact solved separately. Appropriate boundary conditions must be imposed on all the boundaries labelled  $\Gamma$  on the figure. In particular, the ‘repeatability condition’ has been enforced on the lateral boundaries of the foundation,  $\Gamma_{sr}$ , by prescribing the displacements in the left–hand of the foundation to be equal to those in the right–hand side.<sup>16,17</sup> The bottom side of the foundation,  $\Gamma_{si}$ , is a ‘transparent’ boundary which allows the prescribed in–coming seismic

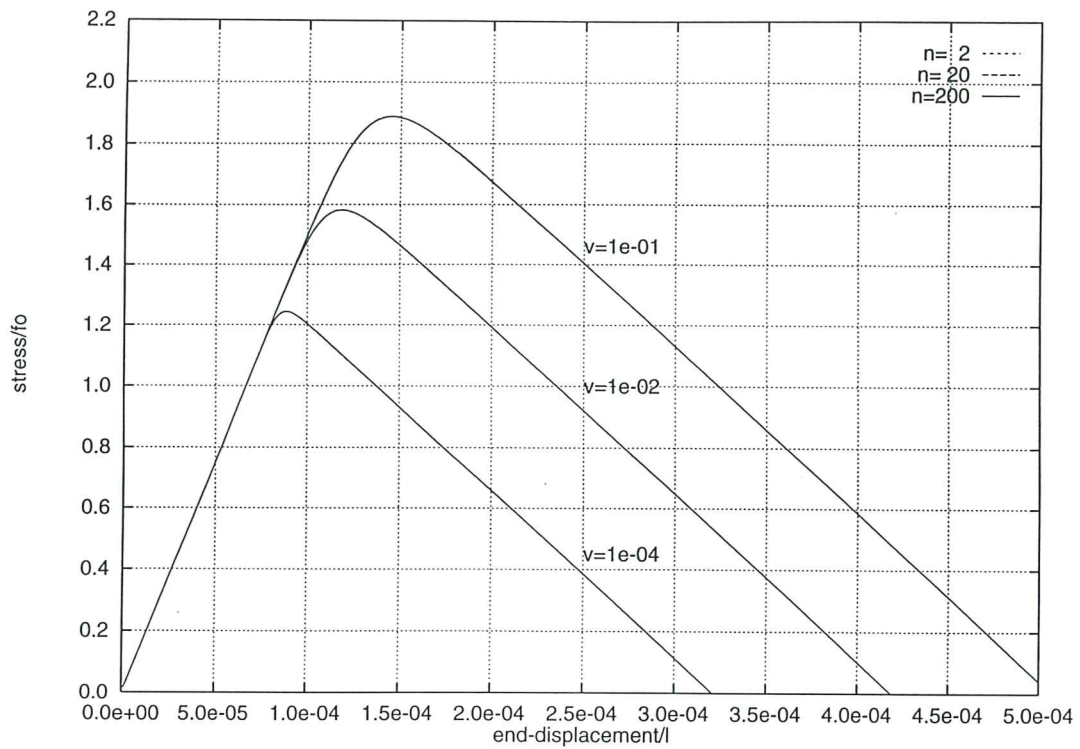


Figure 8. Uniaxial tension test and mesh objectiveness for linear softening law

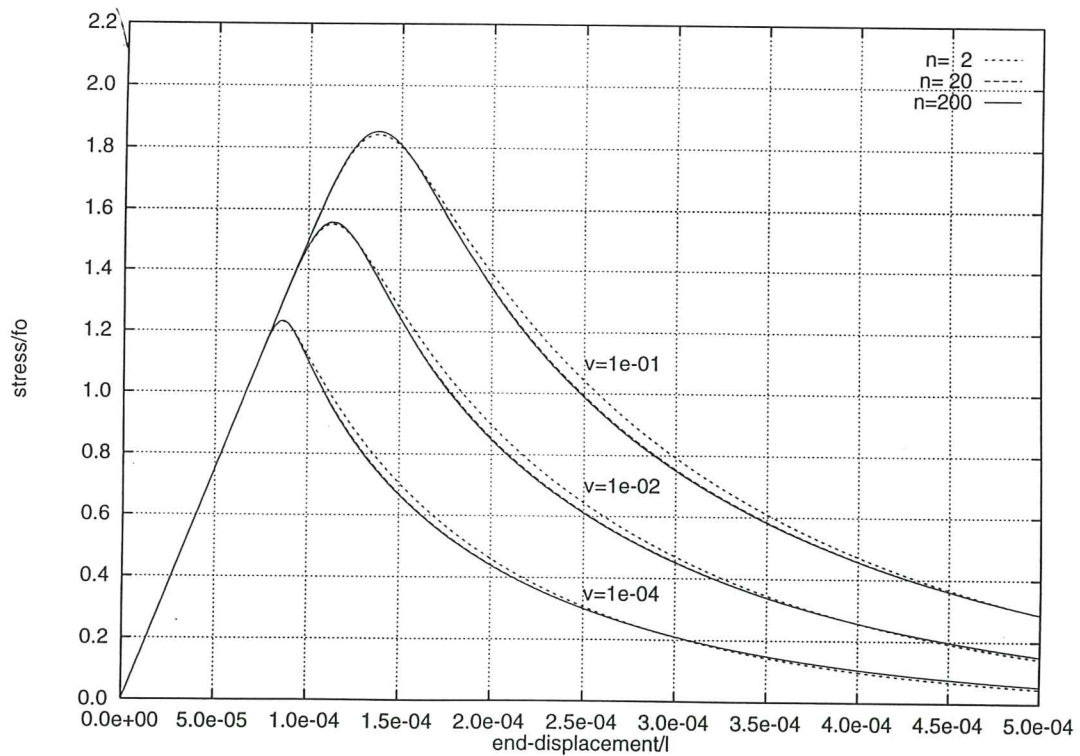


Figure 9. Uniaxial tension test and mesh objectiveness for exponential softening law

wave to enter the domain and propagate vertically towards the dam, and simultaneously, it allows the reflected out-going waves travelling downwards to leave the domain without spurious reflections. The boundaries labelled  $\Gamma_{sf}$  and  $\Gamma_{fs}$  are ‘interaction boundaries’ where fluid–solid interaction is enforced. The fluid free surface,  $\Gamma_{ff}$ , is modelled imposing zero pressure, and the fluid lateral boundary,  $\Gamma_{fr}$ , is a ‘transparent’ boundary which allows the out-going pressure waves to leave the domain without spurious reflections. The detail of the actual procedures used to account for fluid–structure interaction, as well as the imposition of the boundary conditions and input of the seismic action will not be described here. The interested reader may refer to reference 16, where the same problem was considered. The dam selected resembles very closely Koyna Dam in India (107 m high) that has been studied by many researchers interested in seismic analysis. Mostly quadrilateral 4-noded elements are used for the solid and fluid meshes, with triangular 3-noded elements in the refined zone where the non-linear behaviour is expected (see Figure (10.b)).

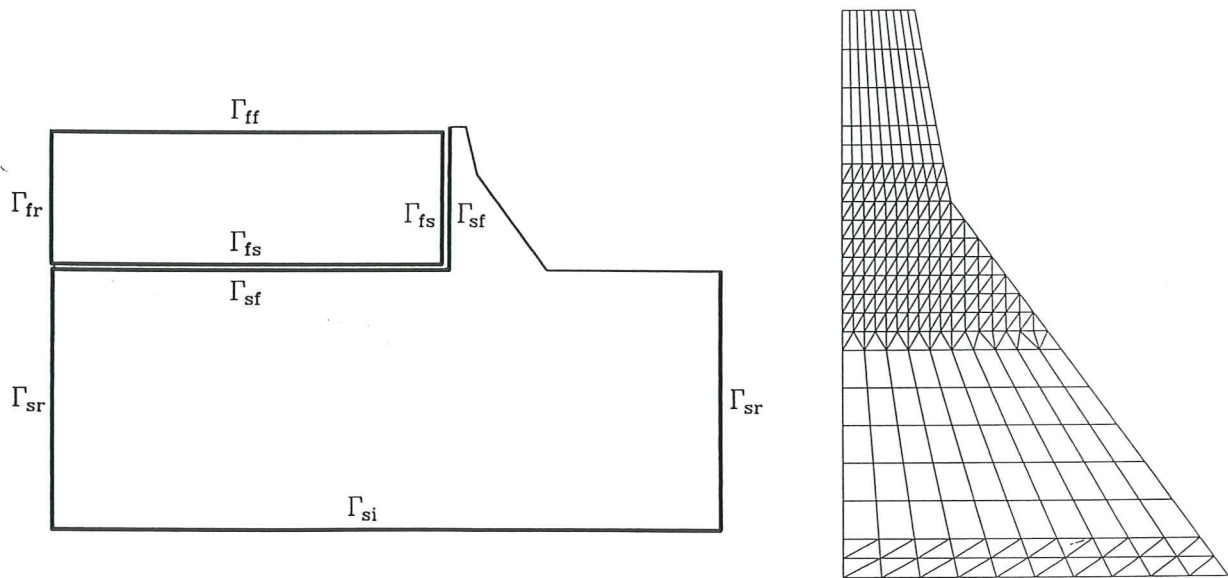


Figure 10. Koyna Dam. (a) Computational model showing the dam with the foundation and the reservoir. (b) Computational mesh used for the dam

The material properties for the concrete of the dam are the same used for the previous examples, with density  $\rho_s = 2600 \text{ kg/m}^3$ . The soil is considered elastic with  $E = 10 \text{ GPa}$ ,  $\nu = 0.2$  and  $\rho_s = 1830 \text{ kg/m}^3$ . With this geometry and material properties, the four largest vibration periods of the dam–foundation system are:  $T_1 = 0.585 \text{ s}$ ,  $T_2 = 0.438 \text{ s}$ ,  $T_3 = 0.353 \text{ s}$  and  $T_4 = 0.291 \text{ s}$ . The four largest vibration periods of the dam on a rigid foundation are:  $T_1 = 0.315 \text{ s}$ ,  $T_2 = 0.121 \text{ s}$ ,  $T_3 = 0.009 \text{ s}$  and  $T_4 = 0.006 \text{ s}$ . This compares well with the results obtained in reference 18, where a very close geometry was considered. The natural damping is tuned to provide a damping ratio of 5 % for the first and second modes of the dam–soil system (Rayleigh parameters  $a = 0.8 \text{ s}^{-1}$ ,  $b = 0.003 \text{ s}$ ). The water

level in the reservoir is 100 *m*. The fluid properties are  $\rho_f = 1019 \text{ kg/m}^3$  and  $c = 1439 \text{ m/s}$  (speed of acoustic waves).

With the objective of analysing the response of this large concrete dam subjected to seismic action an artificial velocigram has been generated.<sup>17</sup> The generated velocigram has a total duration of 10 seconds, with a peak ground acceleration of 0.400*g* and maximum ground velocities around 0.40 *m/s* (occurring about  $t = 3.7 \text{ s}$ ). The dominant period of the signal is 0.4 *s*. The corresponding signal is applied as an horizontal seismic excitation along the canyon direction. The time step used for the analyses is  $\Delta t = 0.002 \text{ s}$ ., with a 0.1% tolerance on residual forces over total forces. The analyses are performed using the rate-dependent damage model presented in this work with material properties  $\bar{\nu}^+ = 870 \text{ s}^{-1}$  and  $a^+ = 5$  (no compression damage ever arises), and repeated for the rate-independent damage model. This allows to evaluate the importance of the rate-effects accounted for with the viscous model in a seismic analysis like this one.

Figure 11 shows the computed horizontal displacements at the top of the dam (relative to the ground) for the two models. Although non-linear effects are significant for this seismic intensity, the displacement response for the two models appears to be very similar. The difference is greater for the vertical component of the displacements (not shown), but the magnitude of this is quite small (less than 1 *cm*). This non-linear effects are evident in Figure 12, which depicts the evolution with time of the mean square value of the tension damage on the dam,  $\bar{d}^+$ . Here the difference between the rate-dependent and independent models is more clearly appreciated, with final values  $\bar{d}^+ = 0.227$  for the rate-independent model and  $\bar{d}^+ = 0.166$  for the rate-dependent model. Note that the evolution of damage is mostly concentrated in a few intervals of time where the maximum positive and negative displacements occur (close to  $t = 1.6 \text{ s}$ .,  $t = 3.2 \text{ s}$ . and  $t = 4.0 \text{ s}$ .).

The evolution of damage with time is again shown in Figures 13 and 14, which show the distribution of damage at selected times ( $t = 3.0 \text{ s}$ .,  $t = 4.0 \text{ s}$ .,  $t = 4.5 \text{ s}$ . and  $t = 12.0 \text{ s}$ .) for both analyses. For the rate-independent model the tensile damage is localised in a zone that almost bridges across the ‘neck’ of the dam. It is initiated firstly at the up-stream wall and then it appears at the down-stream wall and it propagates inwards while the maximum amplitude oscillations occur (between  $t = 3.0 - 4.5 \text{ s}$ .). However, global structural collapse does not occur, as the up-stream and down-stream faces are never under tensile stress at the same time, and the dam retains its overall stability at all times. This is consistent with the results obtained by other researchers using rate-independent damage models.<sup>18</sup>

For the rate-dependent model damage develops in a similar fashion, but the rate-straining is high enough to avoid the progression of damage at mid-height of the up-stream wall at time  $t = 1.685 \text{ s}$ ., and it does not develop afterwards. This difference in the behaviour can be explained by Figure 15, which shows the evolution of the first principal stress precisely for the element situated in that location. For the rate-independent model the stress exceeds the tensile strength of  $f_0^+ = 2.0 \text{ MPa}$  and the element is damaged completely and instantaneously. For the rate-dependent model, the attainable stress is higher, and damage does not occur at that time, even though the stress reaches a value over 2.5 *MPa*. Figure 16 shows how the strain-rate evolves with time at this element for the rate-dependent model. Note that strain-rates  $\dot{\epsilon} > 10^{-3} \text{ s}^{-1}$  occur. According to

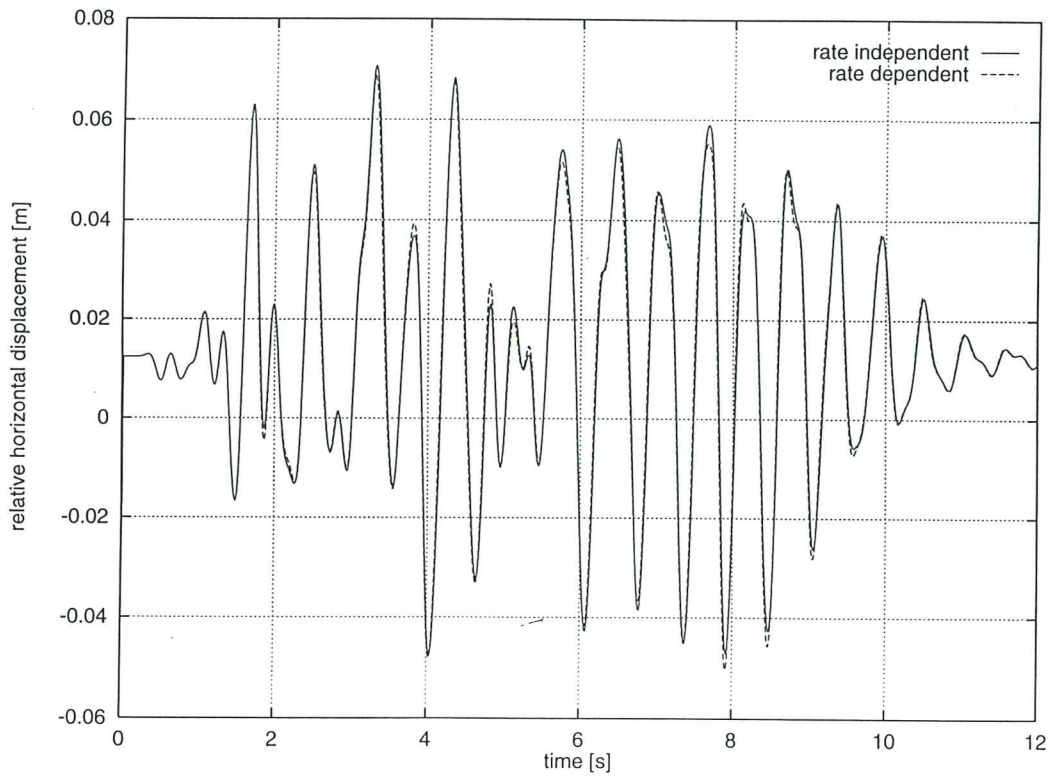


Figure 11. Koyna Dam. Horizontal (relative) displacement at the top of the dam

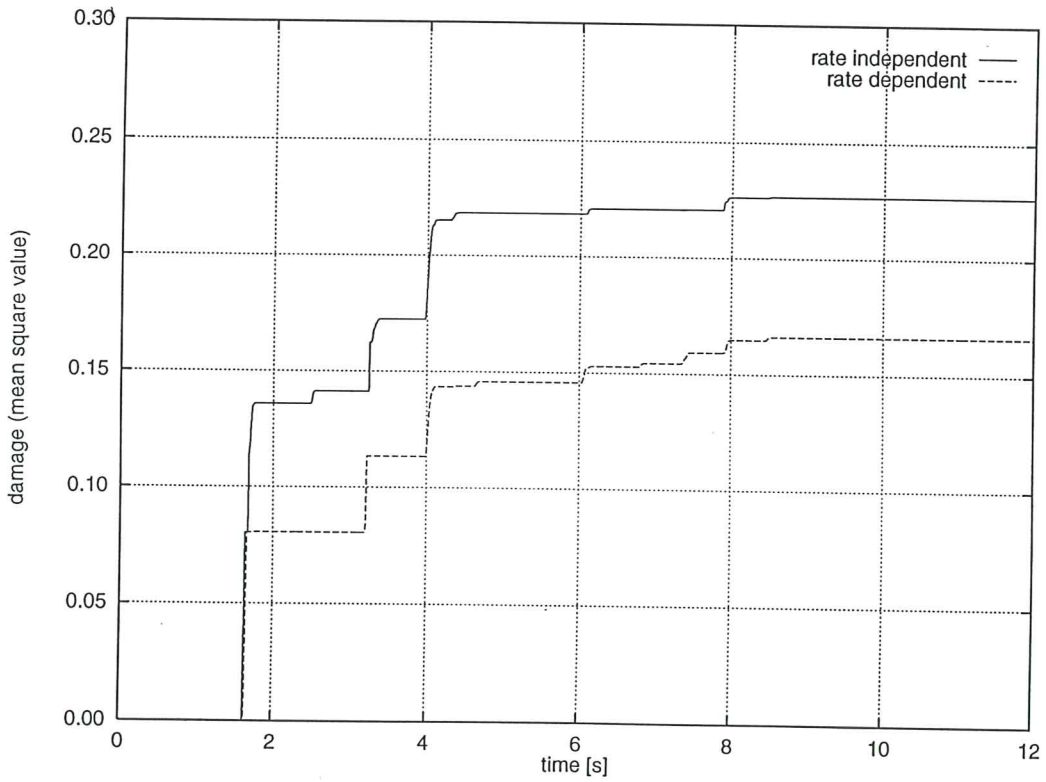


Figure 12. Koyna Dam. Evolution of the tensile damage index (mean square value)

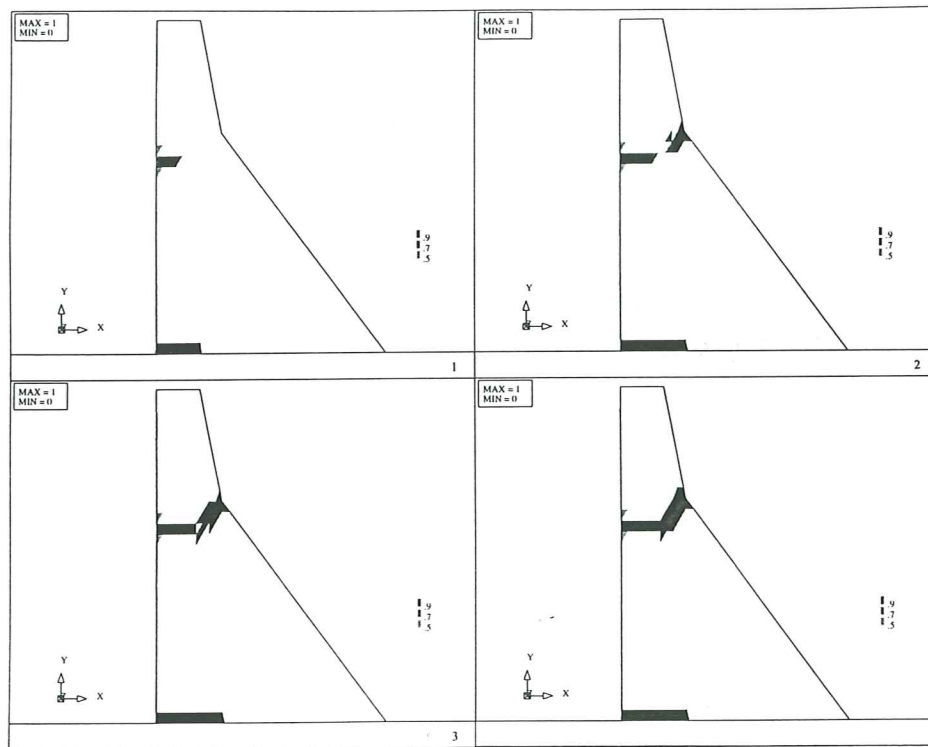


Figure 13. Koyna Dam. Evolution of the tensile damage for the rate-independent model ( $t = 3.0$  s.,  $t = 4.0$  s.,  $t = 4.5$  s. and  $t = 12.0$  s.)

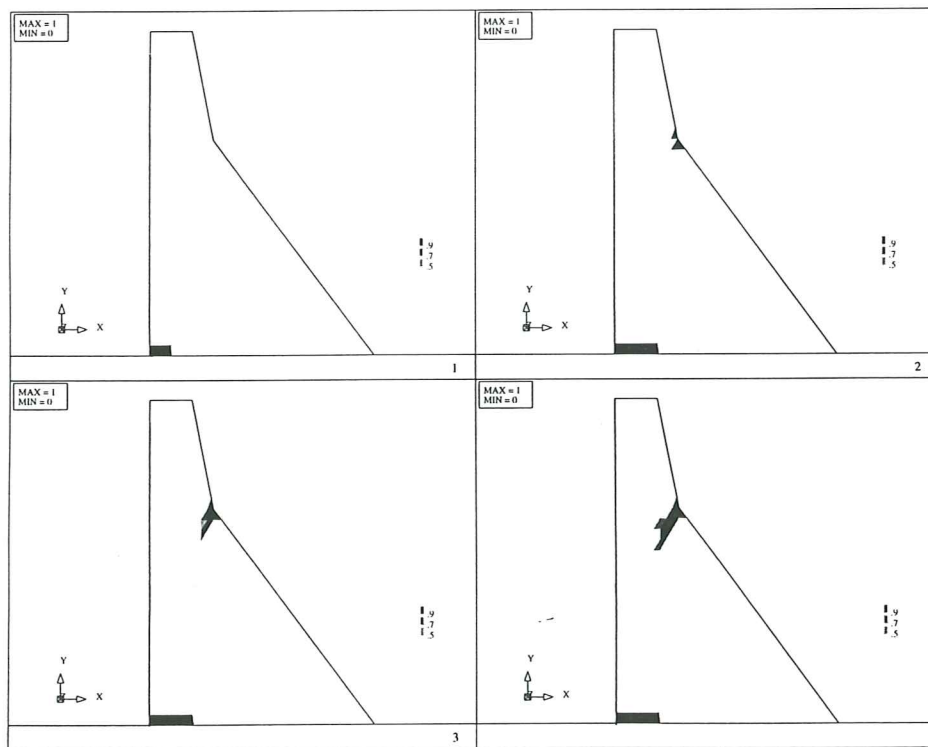


Figure 14. Koyna Dam. Evolution of the tensile damage for the rate-dependent model ( $t = 3.0$  s.,  $t = 4.0$  s.,  $t = 4.5$  s. and  $t = 12.0$  s.)

Figure 5 this would translate in an increase of the strength between 30 and 50 %, which would account for the different behaviour.

The relative importance of the inclusion of rate-sensitivity in the constitutive model is also established by computing the largest eigen-values of the dam-soil system after the seismic analysis, that is, when damage has already developed. For the rate-independent model, these are:  $T_1 = 0.634$  s,  $T_2 = 0.507$  s,  $T_3 = 0.359$  s and  $T_4 = 0.300$  s. For the rate-dependent model, these are:  $T_1 = 0.608$  s,  $T_2 = 0.479$  s,  $T_3 = 0.355$  s and  $T_4 = 0.293$  s. Naturally, the non-linear behaviour results in larger vibration periods for the damaged dam. Note that the first two fundamental modes are the most affected, while the others change comparatively little. The first mode changes 8.37 % and 3.93 %, respectively, while the second changes 15.75 % and 9.36 %. These differences are justified by the different damage maps shown in Figures 13 and 14, which would clearly affect the first and, more substantially, the second vibration modes.

It has been customary for many years to account for the strain-rate effects in a simplistic manner by increasing the values of the ‘static’ tensile strength and fracture energy by a certain percentage, evaluated heuristically. We have found that for this particular example an increase of 45 % in these values produces results, using the rate-independent model, which are extremely close to those of the rate-dependent model. This is consistent with the strain-rates computed for this case, but it cannot be easily extrapolated to other situations.

## 7. CONCLUSIONS

The paper presents an isotropic damage model developed for the numerical analysis of concrete dams subjected to seismic excitation. The model is first introduced in a rate-independent format which incorporates two separate internal variables to characterize damage under tension and compression. This is an essential feature for seismic analysis, as it allows the stiffness regradation upon load reversals. Secondly, a viscous regularization of the model is presented to incorporate a second important feature: rate-sensitivity. The issue of mesh-objectivity when strain-softening occurs is addressed using the concept of the ‘characteristic length’ of the fracture zone, and it is shown that both the softening modulus and the fluidity parameter must depend on it to provide consistent results as the computational mesh is refined. Some aspects of the numerical implementation of the model are also treated, to show that both formats of the model can be easily incorporated in any standard non-linear finite element code prepared to perform structural analysis using a step-by-step time integration method. The resultant model proves to be a good candidate for the numerical simulation of fracture processes in concrete. On one hand, it is firmly founded on consistent constitutive theory, and it is free from empirical factors of difficult physical interpretation. On the other hand, the simplicity of the formulation and the explicitness of the integration of the constitutive equation make it ideally suited for large scale computations. The application of the proposed model to the seismic analysis on a large gravity concrete dam shows the relative importance of the inclusion of rate-sensitivity. It is found that the structural response is not greatly affected in terms of the computed displacement history, but it may vary significantly in terms of the development



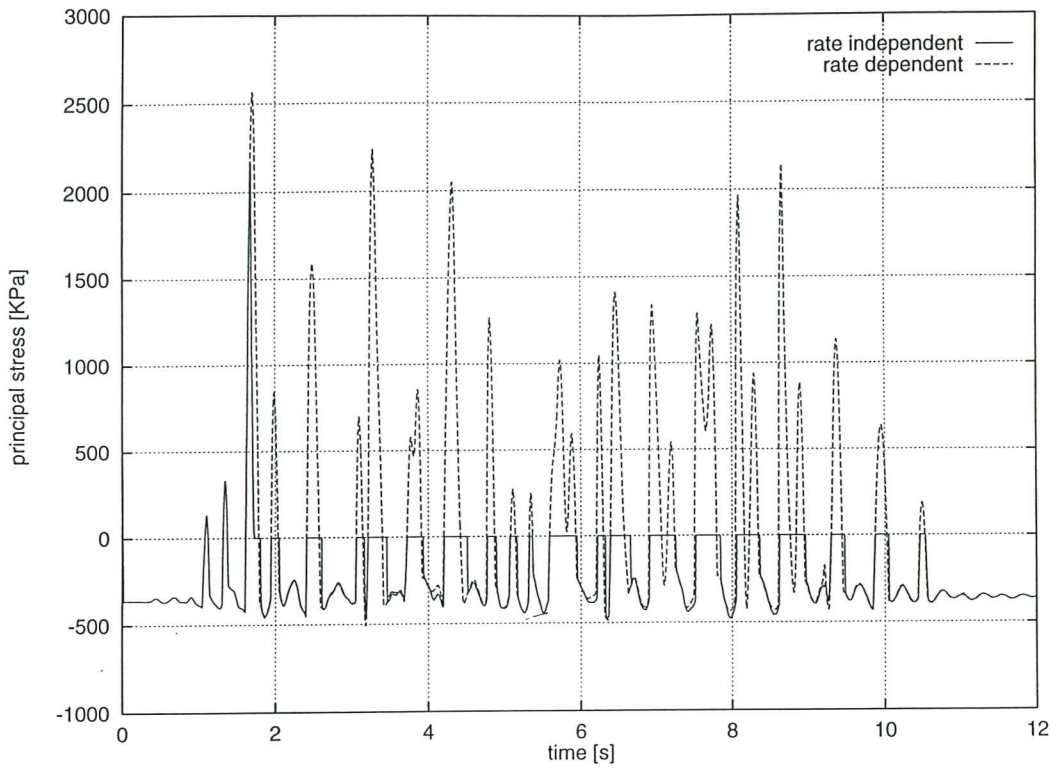


Figure 15. Koyna Dam. Evolution of the first principal stress at the up-stream wall of the dam

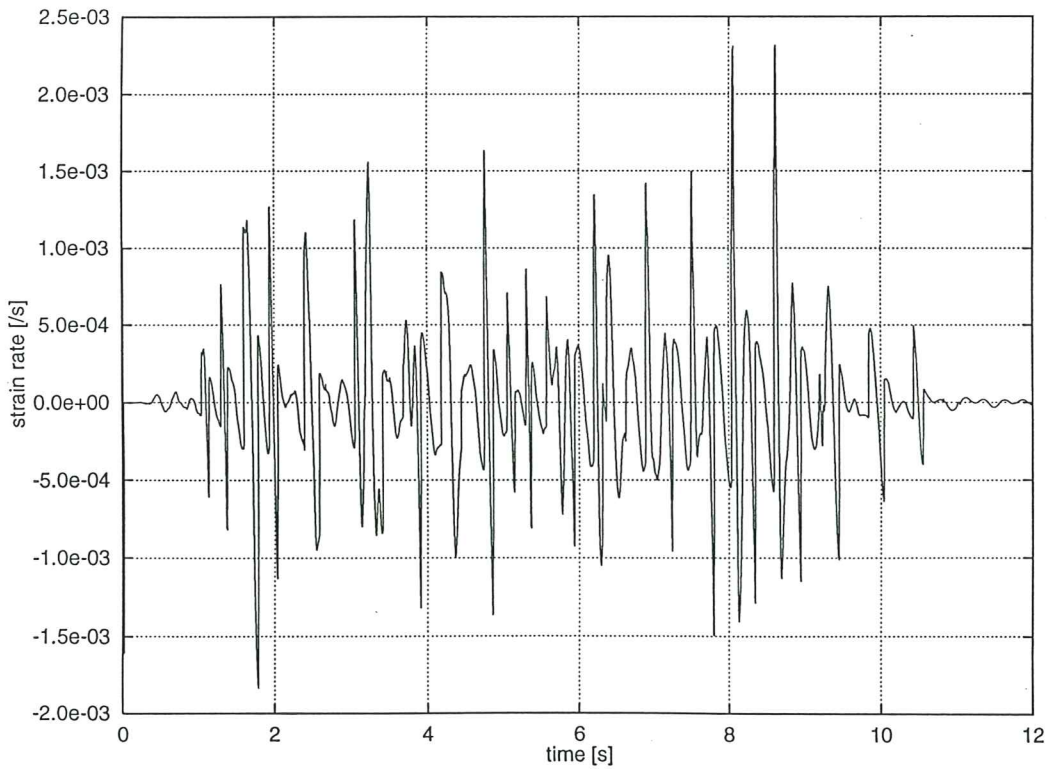


Figure 16. Koyna Dam. Evolution of strain-rate at the up-stream wall of the dam (rate-dependent model)

of damage. The inclusion of rate-sensitivity via viscous regularization is able to reproduce the experimental observation that the tensile peak strength of concrete can be increased up to 50 % for the range of strain-rates that appear in a structural safety analysis of a dam subjected to seismic actions. To conclude, the application of the proposed isotropic continuum damage model to the seismic analysis of a concrete dam shows that it is a useful tool for earthquake engineering and structural dynamic analysis.

#### REFERENCES

1. P. Chappuis, *Modélisation Non-Linéaire du Comportement du Béton sous des Sollicitations Dynamiques*. Doctoral Thesis, Swiss Federal Institute of Technology (1987).
2. N. Bićanić and O.C. Zienkiewicz, 'Constitutive Model for Concrete under Dynamic Loading.' *Earth. Engng. Struc. Dyn.*, **11**, 689–710 (1983).
3. W. Suaris and S. P. Shah, 'Properties of Concrete Subjected to Impact'. *J. of Eng. Mech., ASCE*, **109**, 1727–1741 (1983).
4. W. Suaris and S. P. Shah, 'Rate-Sensitive Damage Theory for Brittle Solids'. *J. of Eng. Mech., ASCE*, **110**, 985–997 (1984).
5. W. Suaris and S. P. Shah, 'Constitutive Model for Dynamic Loading of Concrete'. *J. of Eng. Mech., ASCE*, **111**, 563–576 (1985).
6. W. Suaris, C. Ouyang and V. M. Fernando, 'Damage Model for Cyclic Loading of Concrete'. *J. of Eng. Mech., ASCE*, **116**, 1020–1035 (1990).
7. H.W. Reinhardt and J. Weerheijm, 'Tensile fracture of concrete at high loading rates taking into account of inertia and crack velocity effects'. *Int. J. of Fracture*, **51**, 31–42 (1991).
8. J. Lemaitre and J. L. Chaboche, 'Aspects Phénoménologiques de la Rupture par Endommagement'. *J. Méc. Appl.*, **2**, 317–365 (1978).
9. R. Faria and J. Oliver, *A Rate Dependent Plastic–Damage Constitutive Model for Large Scale Computations in Concrete Structures*. Monography CIMNE, N. 17. (1993).
10. I. Carol and K. Willam, 'Microcrack Opening/Closure Effects in Elastic-Degrading Models'. *Proc. US-Europe Workshop on Fracture and Damage in Quasibrittle Structures.*, 41–52, E&FN Spon (1994).
11. J. Oliver, 'Continuum Modelling of Strong Discontinuities in Solid Mechanics'. *Proc. IV International Conference on Computational Plasticity.*, 455–479, CIMNE (1995).
12. J. C. Simo and J. W. Ju, 'Strain- and Stress-Based Continuum Damage Models – I. Formulation'. *Int. J. Solids Structures*, **23**, 821–840 (1987).
13. J. Oliver, M. Cervera, S. Oller and J. Lubliner, 'Isotropic Damage Models and Smeared Crack Analysis of Concrete'. *Proc. 2nd Int. Conf. on Computer Aided Analysis and Design of Concrete Structures.*, 945–957, Pineridge Press (1990).
14. J. Oliver, 'A Consistent Characteristic Length for Smeared Cracking Models'. *Int. J. Num. Meth. Eng.*, **28**, 461–474 (1985).
15. N. Bićanić and Pankaj. 'Some Computational Aspects of Tensile Strain Localization Modelling in Concrete'. *Engineering Fracture Mechanics*, **35**, 697–708 (1990).
16. M. Cervera, J. Oliver and R. Faria, 'Seismic Evaluation of Concrete Dams via Continuum Damage Models.' *Earth. Engng. Struc. Dyn.*, **24**, 1225–1245 (1995).
17. M. Galindo, *Una metodología para el análisis numérico del comportamiento resistente no lineal de presas de hormigón con cargas estáticas y dinámicas*. Doctoral Thesis, Technical University of Catalonia (1993).
18. F. Ghrib and R. Tinawi, 'An Application of Damage Mechanics for Seismic Analysis of Concrete Gravity Dams.' *Earth. Engng. Struc. Dyn.*, **24**, 157–173 (1995).



## APPENDIX

### ANALYSIS OF DISSIPATION FOR RATE-DEPENDENT DAMAGE MODEL

The analysis of dissipation for the rate-dependent damage model introduced in this work will be carried out by means of the concept of the specific dissipated energy in an uniaxial tension test<sup>13</sup>:

$$g^+ = \int_0^\infty \dot{\gamma} dt \quad (\text{A.1})$$

It follows from the stress expression, Eq. (3.a), that the rate of dissipation in a pure tension test would be:

$$\dot{\gamma} = \Psi_0^+ \dot{d}^+ = \Psi_0^+ \frac{dG^+}{dr^+} \frac{dr^+}{dt} = \Psi_0^+ (G^+)' \dot{r}^+ \quad (\text{A.2})$$

where  $\Psi_0^+$  is the tensile energy potential,  $\dot{d}^+$  is the rate of damage in tension and Eq. (10.a) has been used. Given the definition of  $\Psi_0^+$  and that of the *tensile equivalent stress*,  $\bar{\tau}^+$  (see Eq. (4.a)), it is clear that:

$$\Psi_0^+ = \frac{1}{2} \bar{\sigma}^+ : \mathbf{D}_0^{-1} : \bar{\sigma}^+ = \frac{(\bar{\tau}^+)^2}{2} \quad (\text{A.3})$$

Superscript (+) will be dropped in the following for simplicity.

On the other hand, for monotone-increasing straining, Eqs. (10.a) and (11.a) can be combined to yield:

$$\bar{\tau} = \left[ 1 + \left( \frac{\dot{r}}{r_0 \vartheta} \right)^{\frac{1}{a}} \right] r \quad (\text{A.4})$$

Substitution of (A.4), (A.3) and (A.2) into (A.1) gives

$$g = \int_0^\infty \frac{1}{2} \left[ 1 + \left( \frac{\dot{r}}{r_0 \vartheta} \right)^{\frac{1}{a}} \right]^2 r^2 G' \dot{r} dt \quad (\text{A.5})$$

Let us consider the energy  $g$  dissipated per unit volume over a domain which has a ‘typical width’  $l_{ch}$  (the ‘characteristic length’) be expressed as:

$$g = \frac{\bar{g}}{l_{ch}} \quad (\text{A.6})$$

with  $\bar{g}$  having the meaning of dissipated energy per unit of surface. Let us assume that  $\bar{g}$  depends on the material properties and on the rate of straining, but it is independent on  $l_{ch}$ .

Let us now consider the situation depicted in Figure 7 for the uniaxial tension test. This test is carried out by imposing a free-end displacement  $\delta = \delta(t)$  as an *arbitrary* monotone-increasing function of time, and with  $\delta(t=0) = f_0 l/E$ , so that  $t=0$  is the time for the onset of damage. We expect the damage to develop in a band equal to  $l_{ch}$  (one element of

the mesh in a numerical simulation of the test). Let us denote by  $\varepsilon_d$  the strain within the localization band and by  $\varepsilon_e$  the (elastic) strain outside this band. Equilibrium of tractions along the bar allows to express

$$\varepsilon_e = (1 - d) \varepsilon_d \quad (\text{A.7})$$

Boundary conditions demand that at any time

$$\delta = \varepsilon_d l_{ch} + \varepsilon_e (l - l_{ch}) \quad (\text{A.8})$$

Therefore, from (A.7) and (A.8)

$$\varepsilon_d = \frac{\delta}{l_{ch} + (1 - d)(l - l_{ch})} \quad (\text{A.9})$$

As for the uniaxial problem  $\bar{\tau}^2 = E \varepsilon_d^2$  in the damaged zone, (A.4) can be used to yield

$$\left[ 1 + \left( \frac{\dot{r}}{r_0 \vartheta} \right)^{\frac{1}{a}} \right] r = \frac{\sqrt{E} \delta(t)}{l_{ch} + (1 - d)(l - l_{ch})} \quad (\text{A.10})$$

As  $d = G(r)$ , (A.10) is a differential equation which can be solved for  $r$ , with the initial condition  $r(t = 0) = r_0$ .

#### A.1 Linear softening law

Let us assume in the following a *linear* law for softening, which would correspond to a function  $G$  for the evolution of damage of the form

$$d = G(r) = \frac{1}{1 - H} \left( 1 - \frac{r_0}{r} \right) \quad r_0 \leq r \leq r_u \quad (\text{A.11})$$

where  $H \geq 0$  is the softening modulus,  $r_0 = f_0/\sqrt{E}$  and  $r_u = r_0/H$ . Let us first consider the uniaxial tension test carried out under ‘quasi-static’ conditions, that is, with  $\dot{r} = 0$ . Now Eq. (A.5) can be particularized and integrated to give

$$g_{qst} = \int_{r_0}^{r_u} \frac{1}{2} \left( \frac{r_0}{1 - H} \right) dr = \frac{r_0^2}{2H} \quad (\text{A.12})$$

Imposing now condition (A.6), which for this particular case can be expressed as  $g_{qst} = G_f/l_{ch}$ ,  $G_f$  being the so-called ‘fracture energy’ of the material, the softening modulus is found to be:

$$H = \frac{r_0^2 l_{ch}}{2 G_f} = \bar{H} l_{ch} \quad (\text{A.13})$$

where  $\bar{H}$  is a material property. The additional condition  $\dot{d}(t = 0) = \frac{1}{1 - H} \frac{\dot{r}}{r_0} \geq 0$  imposes that  $H \leq 1$ , which yields the well-known limitation on  $l_{ch}$ :

$$l_{ch} \leq \frac{1}{\bar{H}} = \frac{2 G_f}{r_0^2} \quad (\text{A.14})$$

Let us now consider the uniaxial tension test carried out under ‘rate-dependent’ conditions, that is, with  $\dot{r} \neq 0$ . Now Eq. (A.5) can be particularized to give

$$g_{rate} = \int_{r_0}^{r_u} \frac{1}{2} \left[ 1 + \left( \frac{\dot{r}}{r_0 \vartheta} \right)^{\frac{1}{a}} \right]^2 \left( \frac{r_0}{1-H} \right) dr \quad (\text{A.15})$$

Let us introduce the new variable  $s = (r - r_0)/r_0 \vartheta$ , so that (A.15) can be rewritten as

$$g_{rate} = \int_0^{s_u} \frac{1}{2} \left[ 1 + (\dot{s})^{\frac{1}{a}} \right]^2 \left( \frac{r_0^2 \vartheta}{1-H} \right) ds \quad (\text{A.16})$$

For  $g_{rate}$  in (A.16) to have the appropriate form (A.6),  $\vartheta$  must be of the form

$$\vartheta = \bar{\vartheta} \left( \frac{1}{l_{ch}} - \bar{H} \right) \geq 0 \quad (\text{A.17})$$

where  $\bar{\vartheta}$  is a material property. Now  $s_u = 1/\bar{H}\bar{\vartheta}$  and (A.16) can be simplified to be

$$g_{rate} = \int_0^{s_u} \frac{1}{2} \left[ 1 + (\dot{s})^{\frac{1}{a}} \right]^2 \frac{r_0^2 \bar{\vartheta}}{l_{ch}} ds \quad (\text{A.18})$$

It is easy to see that  $g_{rate}$  in (A.18) will have the appropriate form if the bracketed term inside the integral does not depend on  $l_{ch}$ . To show that this is the case, let us introduce the softening law (A.11) in the differential equation (A.10). Some manipulation leads to the particularized equation (in terms of the new variable  $s$ ):

$$\left[ 1 + (\dot{s})^{\frac{1}{a}} \right] [C\vartheta s + l] = \frac{E}{f_0} \delta(t) \quad (\text{A.19})$$

with the initial condition  $s(t = 0) = 0$ . In (A.19)  $C = (1 - \bar{H}l)/(1/l_{ch} - \bar{H})$ , and therefore, in view of (A.17), the product  $C\vartheta$  does not depend on  $l_{ch}$ . Thus, it is clear that Eq. (A.19) does not depend on  $l_{ch}$ . The response  $s = s(t)$  is mesh-objective, and so will be the dissipated energy  $\bar{g}_{rate} = g_{rate} l_{ch}$ , as desired.

Remarks:

- (i) For  $\bar{H}, \bar{\vartheta} \geq 0$ , the condition  $\vartheta \geq 0$  does not impose a different upper limit on  $l_{ch}$  from that on (A.14).
- (ii) The specific dissipation energy  $\bar{g}_{rate}$  can be related to the ‘static’ fracture energy of the material in the form  $\bar{g}_{rate} = g_{rate} l_{ch} = \alpha_{rate} G_f$ , with  $\alpha_{rate} \geq 1$  being a ‘magnification factor’ which depends on the rate of straining and the properties of the material. Its appearance agrees with the experimental observation that ‘fracture energy’ is larger at larger strain-rates.
- (iii) Mesh objectivity is achieved for any *arbitrary* monotone-increasing function  $\delta(t)$ .

## A.2 Exponential softening law

Let us assume in the following an *exponential* law for softening, which would correspond to a function  $G$  for the evolution of damage of the form

$$d = G(r) = 1 - \frac{r_0}{r} e^{A(1-\frac{r}{r_0})} \quad r_0 \leq r \leq \infty \quad (\text{A.20})$$

where  $A \geq 0$  plays the role of the softening modulus and  $r_0 = f_0/\sqrt{E}$ . Let us first consider the uniaxial tension test carried out under ‘quasi-static’ conditions, that is, with  $\dot{r} = 0$ . Now Eq. (A.5) can be particularized to give

$$g_{qst} = \int_{r_0}^{\infty} \frac{1}{2} (r_0 + Ar) e^{A(1-\frac{r}{r_0})} dr = \frac{1}{2} \left(1 + \frac{2}{A}\right) r_0^2 \quad (\text{A.21})$$

Imposing now condition (A.6),  $g_{qst} = G_f / l_{ch}$ , the softening modulus  $A$  is found to be:

$$\frac{1}{A} = \frac{1}{2\overline{H}} \left( \frac{1}{l_{ch}} - \overline{H} \right) \geq 0 \quad (\text{A.22})$$

where  $\overline{H}$  is a material property defined above. The condition  $A \geq 0$  imposes the same upper limit on  $l_{ch}$  as Eqs. (A.14) and (A.17).

Let us now consider the uniaxial tension test carried out under ‘rate-dependent’ conditions, that is, with  $\dot{r} \neq 0$ . Now Eq. (A.5) can be particularized to give

$$g_{rate} = \int_{r_0}^{\infty} \frac{1}{2} \left[ 1 + \left( \frac{\dot{r}}{r_0 \vartheta} \right)^{\frac{1}{a}} \right]^2 (r_0 + Ar) e^{A(1-\frac{r}{r_0})} dr \quad (\text{A.23})$$

Due to the complicated expression of (A.23), it does not seem possible to establish a general condition for  $g_{rate}$  to have the appropriate form and, therefore, to ensure mesh objectivity. However, let us consider the situation *on mesh refinement*, that is, as  $l_{ch}$  reduces and tends to zero (and so does  $A$ , see (A.22)). Now it is possible to expand (A.20) in a Taylor’s series around the value  $A = 0$ , and retain only up to the linear term to have

$$d = (1 + A) \left( 1 - \frac{r_0}{r} \right) \quad r_0 \leq r \leq r_u \quad (\text{A.24})$$

where  $r_u = r_0(1 + A)/A$ . Eq. (A.24) represents the linear softening law which approximates the exponential law (A.20) as  $l_{ch}$  tends to zero. The analysis already performed for the linear law allows to conclude that if  $\vartheta$  has the form of Eq. (A.17) mesh objectivity will also be achieved for the exponential softening law if the localization band is sufficiently small (on mesh refinement).

In fact, the procedure followed allows to conclude that if  $\vartheta$  has the form of Eq. (A.17) mesh objectivity will be achieved for any softening law *on mesh refinement*.